

Microbubble Expansion in a Flexible Tube

Tao Ye

Joseph L. Bull
e-mail: joebull@umich.edu

Biomedical Engineering Department,
The University of Michigan,
Ann Arbor, MI 48109

We have utilized a computational model of the expansion of a microbubble in a liquid-filled flexible tube to investigate the potential for acoustic vaporization of perfluorocarbon droplets to damage blood vessels during a novel gas embolotherapy technique for the potential treatment of tumors. This model uses a fixed grid, multi-domain, interface tracking, direct numerical simulation method that treats all interfaces and boundaries as sharp discontinuities for high accuracy. In the current work, we examined effects of initial bubble size on the flows and wall stresses that result from droplet vaporization. The remaining dimensionless parameters that govern the system response (Reynolds, Weber, and Strouhal numbers, initial bubble pressure, and wall stiffness and tension) were selected to model an arteriole. The results for a flexible tube are significantly different from those for a rigid tube. Two major flow regimes occur due to the combined effect of bubble and tube deformation: in flow at the tube ends and out flow near the bubble surface. The flexibility of the tube largely dissipates the extreme pressure that develops in the rigid tube model. Both the magnitude and the overall expansion time of the rapidly changing pressure are greatly reduced in the flexible tube. Smaller initial bubble diameters, relative to the vessel diameter, result in lower wall stresses. This study indicates that wall flexibility can significantly influence the wall stresses that result from acoustic vaporization of intravascular perfluorocarbon droplets, and suggests that acoustic activation of droplets in larger, more flexible vessels may be less likely to damage or rupture vessels than activation in smaller and stiffer vessels. [DOI: 10.1115/1.2206200]

1 Introduction

Microbubbles are relevant to a number of clinical situations including disease conditions, such as air embolism [1–10], and therapeutic and diagnostic interventions [1]. Bubbles scatter ultrasound better than tissue or blood, and contrast agents are often used with ultrasound for diagnostic purposes. For therapeutic applications, we are developing a minimally invasive gas embolotherapy that uses selectively formed perfluorocarbon (PFC) bubbles as emboli, described in detail elsewhere [1] and briefly here. Embolotherapy is a means to treat cancer through the occlusion of blood vessels using foreign bodies. Boehm et al. [11] demonstrated that cancer cells can be starved to death if the blood flow to tumors is blocked. A variety of cancers, such as hepatocellular carcinoma (HCC) and renal carcinoma, have been effectively treated using embolotherapy in conjunction with localized drug delivery [12–14]. HCC is the most common form of liver cancer, occurring in 2–30 per 100,000 males each year, and causes an estimated 1,250,000 deaths worldwide every year. It is difficult to treat by traditional methods because the accompanying liver cirrhosis makes most patients (70–85%) ineligible for treatment by resection [13]. Previous embolotherapy work has primarily used solid emboli, including absorbable materials, such as blood clot, cellulose and gelatin sponge (Gelfoam), or nonabsorbable materials, such as particulates, coils, balloons, and streamers. Solid emboli are normally introduced through intravascular catheters and percutaneously, requiring either surgical exposure of vessels near the target region or very selective catheter placement to minimize embolization of tissue collateral to the tumor. Because of difficulties in directing and confining treatment to the target area, the use of embolotherapy in treating tumors is limited and it is primarily used as a last resort after conventional treatments have failed.

Selective formation and delivery of gas emboli may overcome this limitation associated with solid emboli. In our developmental

gas embolotherapy procedure, albumin-encapsulated DDFP (dodecafluoropentane, C5F12) droplets, 6 μm diameter, are injected into the vasculature and imaged using standard ultrasound. DDFP has a boiling point of 29 °C at atmospheric pressure, but the albumin shell prevents spontaneous vaporization of droplets at body temperature [15–17]. These droplets are small enough that they do not stick in capillaries, and may be injected intravenously. Once they reach the target area they are selectively vaporized under high-intensity ultrasound (acoustic droplet vaporization, ADV) [15–17]. Focused ultrasound allows confinement of ADV to small regions, $O(1 \text{ mm}^2)$ at a depth $O(10 \text{ mm})$ [17]. The selectivity of ADV will depend on the location of the tumor, and the clinical situation will likely be more challenging than the animal experiments. Future development of acoustic arrays is expected to improve selectivity. Although there are likely several possible mechanisms of droplet vaporization and which one occurs may depend on droplet size and acoustic parameters, initial experiments suggest that ultrasound disrupts the albumin shell allowing the superheated liquid PFC to vaporize, rather than cavitating the liquid PFC [15–17]. The resultant bubbles are large enough to occlude blood flow when lodged in the tumor vasculature, and have sufficient persistence times, $O(\text{days})$, to induce infarction. The procedure is minimally invasive and the efficacy of treatment depends on the ability to safely vaporize the droplets and to deliver the resulting bubbles to the desired location so that collateral infarction is minimized. In other studies, we have examined the transport of bubbles in bifurcations, corresponding to bubble transport before lodging occurs [18,19], and transport in bifurcating networks in which bubbles can lodge [20].

ADV is a fast process ($<10^{-6}$ s for vaporization and subsequent bubble expansion) [16], and the rapid volume expansion in the confined space of a blood vessel may potentially result in wall stresses that are sufficient to rupture blood vessels and/or damage the vessel endothelium. Ultrasound-induced collapse of contrast agent microbubbles, a different phenomenon from ADV, has been shown to result in rupture of capillaries [21–23], which can lead to angiogenesis and arteriogenesis [22,23]. Neither of these is a desired effect in gas embolotherapy. Wall stress affects the vascular

Contributed by the Bioengineering Division of ASME for publication in the JOURNAL OF BIOMECHANICAL ENGINEERING. Manuscript received July 27, 2005; final manuscript received January 30, 2006. Review conducted by Cheng Dong.

endothelium and can modify endothelial biology, including morphology, endocytosis, proliferation, and signal transduction mechanisms [24–27]. Vessel wall stress may be a determinant to the distribution and development of atherosclerotic lesions [25,28]. An intact endothelium also provides protection from arterial thrombosis [29].

As noted above, the small size of the droplets is intended to allow venous injection, and the selective application of ultrasound is expected to minimize collateral infarction of healthy tissue. In some instances, it may be desirable to use droplets that are too large for venous injection (due to droplet lodging in systemic or pulmonary capillaries before ever reaching the tumor). The selectivity provided by ADV would likely still provide a significant advantage over conventional embolotherapy. ADV in small arteries feeding a tumor would allow the resulting bubbles to lodge in small arterioles or capillaries within the tumor. In treatment of tumors with less defined or less accessible arterial structure, vaporization of droplets in microvessels would be preferred to minimize collateral infarction. In that scenario, the resulting bubbles would lodge soon after ADV, minimizing the potential for the bubbles to lodge outside the tumor. That strategy is expected to provide more selective delivery than ADV in larger vessels, which would likely require the microbubbles to travel a farther distance along the vascular tree before lodging. A potential disadvantage of vaporization in microvessels is the possibility of bioeffects induced from vaporizing a droplet in a vessel that is only slightly larger in diameter than the droplet.

The objective of our investigation is to model the ADV process and to assess the effects of PFC droplet size on the resulting vessel wall stresses and deformation, which likely determine the potential bioeffects to the vessel. While vessels are flexible in general, the degree of flexibility depends on the size and location of the vessel. Those embedded in the tissue are constrained with little flexibility, and thus can be modeled as rigid tubes. Our previous study [30] presented the stress results for a bubble expanding in a liquid-filled rigid tube. It was found that fluid stress at the wall depends on initial bubble size, surface tension, viscosity, and the initial bubble pressure. Other vessels can have significant deformation due to fluid motion and, thus, cannot be treated as rigid tubes. In this paper, we extend our model to include a flexible tube wall to investigate the flow and stress that ADV induces in more flexible vessels. The modeling of biological flows in flexible tubes is described elsewhere [31–38]. Previous work has considered the motion of long bubbles in flexible tubes as models of airway reopening and surfactant delivery [39–44]. The current study focuses on inertia-driven bubble expansion in a flexible liquid-filled tube and the effects of initial bubble diameter on the resulting fluid stresses at the wall, a previously uninvestigated problem. Direct numerical simulations are conducted to examine the process.

2 Model Formulation

2.1 Geometry and Assumptions. The model geometry and computational domain are shown in Fig. 1. The expansion of a DDFP bubble in a flexible vessel is modeled by a single, bubble initially located at the center of a flexible cylindrical tube. The gas bubble is modeled as an ideal gas, and the surrounding blood is modeled as an incompressible, Newtonian liquid. The tube of length L_t and inner diameter D is filled with liquid, which is initially at rest. Flow pulsatility and both time dependent and convective inertial effects are small in the microcirculation [45]. Consequently, vessel wall oscillations are much smaller there than in arteries. The typical blood velocities in arterioles, $O(1 \text{ cm/s})$ [45], are much less than the velocity associated with the expansion of a bubble produced by ADV. Therefore we consider the background blood flow contribution to the velocity field during ADV to be a secondary order effect and focus our attention on the leading order contribution of the bubble expansion by itself by assuming the fluid is initially at rest. The expansion velocity is compared to the

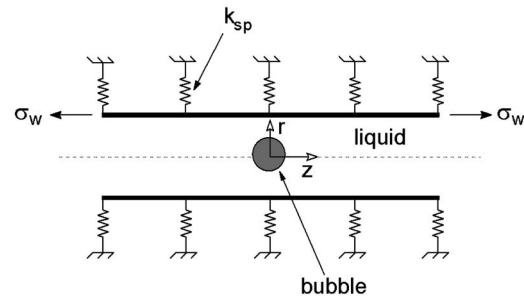


Fig. 1 Schematic of a bubble in a flexible tube. The bubble is located at the center of the tube and its initially high pressure drives the subsequent bubble expansion. The initial bubble size ranges from 10% to 90% of the tube diameter, D . The tube wall is flexible over the entire length, L_t . The tube is characterized by radial stiffness, k_{sp} , and longitudinal tension, σ_w . The tube is filled with a viscous incompressible liquid that is initially at rest. A constant ambient pressure, P_∞ , is specified at the tube exits.

wave speed associated with the flexible tube, which can be thought of as representing an upper limit on background flow speed, in more detail in Sec. 4.

Both ends of the tube open to liquid reservoirs, which are at a constant pressure, P_∞^* . We consider axisymmetry about the centerline of the cylindrical tube and symmetry left to right about the center of the bubble. The computational domain is half of the physical domain. The flexible wall is modeled by radial elasticity, k_{sp} , represented by springs in Fig. 1, and longitudinal wall tension, σ_w . Wall inertia is neglected since we are considering thin-walled arterioles whose wall mass is much less than the liquid mass. It should be noted that inertial effects of tissue surrounding the arteriole could potentially contribute to the resulting behavior. However, significance of this contribution depends on the location of the specific arteriole, and these effects are neglected in this first examination of the effects of wall flexibility.

The vaporization of small PFC droplets ($\sim 6 \mu\text{m}$ diameter) takes place within approximately 10^{-9} s second [16]. This vaporization is then followed by a rapid ($\sim 10^{-6}$ s) expansion of the resulting gas bubble. In gas embolotherapy, we are primarily interested in the bulk effect of the volume increase as a result of the ADV, and the transition of droplets to bubbles is modeled as an initial bubble that has the same volume as the droplet and with a high initial pressure, $P_h^* \gg P_\infty^*$, corresponding to the complete vaporization of the droplet before any expansion. This modeling approach has been used by others [46] and in our previous study [30]. The subsequent bubble expansion is driven by this high pressure. Our simulations focus on the resulting fluid, bubble, and flexible wall evolution. The process is assumed to be isothermal since the bubbles originate from $\sim 6 \mu\text{m}$ droplets whose temperature has equilibrated with that of the surrounding blood. Mass diffusion across the bubble interface after droplet vaporization is not considered, because it is a slow process compared to the expansion investigated in this study, which occurs over a time scale of $\sim 10^{-6}$ s. This time scale is based on ADV experiments of an unconstrained droplet [16], and is consistent with the time scale one obtains from balancing the convective inertia and pressure gradient terms in the Navier-Stokes equation for the tube length we consider here.

2.2 Governing Equations. In the following descriptions, the subscript l stands for liquid phase, v for vapor phase, int for interface, w for wall boundary, n for normal direction at bubble interface or flexible wall pointing from the bubble or tube wall into the liquid, t for tangential direction of the bubble interface or flexible wall, and r for radial component of a vector. Dimensional variables are denoted by superscript $*$. The flow is assumed to be

axisymmetric with no variation in the azimuthal direction and the governing equations have only r and z components in cylindrical coordinates. The liquid is governed by the conservation of mass and momentum (Navier-Stokes) equations. Velocity, density, pressure, and viscosity are denoted by \mathbf{u}^* , ρ , p^* , and μ , respectively. The gas phase is considered inviscid and is represented by the isothermal ideal gas law

$$P_v^* V_v^* = \text{constant} \quad (2.1)$$

where P_v^* is the bubble pressure and V_v^* is the bubble volume. Isothermal expansion of the bubble is assumed because, as noted in Sec. 1, the liquid droplet is superheated at body temperature and its vaporization appears to involve disruption of the albumin shell that prevents it from vaporizing, rather than cavitation within the droplet.

2.3 Boundary and Interfacial Conditions. The fixed boundary conditions specified for solving the Navier-Stokes equation are $p^* = P_\infty^*$ at the tube exits (left and right boundaries in Fig. 1), and symmetry of all variables at the tube centerline. The bubble interface and the tube wall velocities and positions are obtained as part of the solution. At all times, the following dynamic conditions are satisfied on these two moving boundaries.

The bubble is initially spherical in shape, but is not required to remain spherical as its interface evolves in time. It is, however, required to remain axisymmetric about the tube centerline due to the symmetry assumption. The kinematic boundary condition requires the normal components of the bubble interface velocity and the liquid velocity at the interface to be the same, such that

$$\frac{d\mathbf{Y}^*}{dt^*} = (\mathbf{u}_l^* \cdot \hat{n}) \hat{n} \quad (2.2)$$

where \mathbf{Y}^* is the interface position and \hat{n} is the unit normal vector to the interface. In this study, surface tension is assumed constant and the bubble is assumed inviscid, so the stress boundary condition at the interface is

$$p_v^* \hat{n} = p_l^* \hat{n} - \boldsymbol{\tau}_l^* \cdot \hat{n} + \sigma_b \kappa_b^* \hat{n} \quad (2.3)$$

where $\boldsymbol{\tau}_l^*$ is the liquid viscous stress tensor, σ_b is surface tension, and $\kappa_b^* = \nabla^* \cdot \hat{n}$ is interfacial curvature. The normal and tangential components of Eq. (2.3) are

$$p_l^* - p_v^* + \sigma_b \kappa_b^* = (\boldsymbol{\tau}_l^* \cdot \hat{n})_n \quad (2.4)$$

and

$$(\boldsymbol{\tau}_l^* \cdot \hat{n})_t = 0 \quad (2.5)$$

where $(\boldsymbol{\tau}_l^* \cdot \hat{n})_n$ and $(\boldsymbol{\tau}_l^* \cdot \hat{n})_t$ are the normal and tangential components of the liquid viscous stress vector, $\boldsymbol{\tau}_l^* \cdot \hat{n}$, respectively, and \hat{t} is the unit tangent vector to the interface. If the vapor phase is viscous, there is a similar term, $(\boldsymbol{\tau}_v^* \cdot \hat{n})_t$, in the vapor.

The tube wall is initially uniform in radius, but can deform due to the fluid stresses on it. This deformation is coupled to the flow equations. The flexible tube wall is modeled as a structural boundary with zero mass and thickness. The stress-deformation relationship of the wall is represented by radial stiffness and a constant longitudinal tension [39,47]. The radial wall displacement from equilibrium is linearly proportional to the radial component of fluid stress at the wall. The tension element of the structure results in net force in the normal direction of the structure boundary when it is deformed. Hence, the normal stress boundary condition at the tube wall is

$$p_l^* - \mu_l \left(\frac{\partial u_n^*}{\partial n} \right)_l + \sigma_w \kappa_w^* - k_{sp} \Delta r^* = 0 \quad (2.6)$$

where σ_w is wall tension (N/m), κ_w^* is the curvature of the tube wall, k_{sp} is the spring constant (N/m³), Δr^* is the displacement in the radial direction, and n_r is the radial component of the unit normal of the wall. Note that the ends of the tube are not pinned

in the radial direction, and the tube can expand or contract there according to Eq. (2.6).

2.4 Nondimensionalization. The governing equations and boundary conditions are nondimensionalized in terms of L_r , u_r , and $t_r = L_r/u_r$ that are the length scale, velocity scale, and time scale, respectively. Here subscript r denotes reference scales used in the non-dimensionalization process. The dimensionless variables are defined as $\mathbf{x} = \mathbf{x}^*/L_r$, $\mathbf{u} = \mathbf{u}^*/u_r$, $t = t^*/t_r$, $p = p^*/(\rho_l u_r^2)$, where the liquid properties are chosen as the reference properties ($\rho_r = \rho_l$) and the tube diameter is the length scale ($L_r = D$).

The dimensionless mass and momentum conservation equations for the liquid phase are

$$\nabla \cdot \mathbf{u} = 0 \quad (2.7)$$

$$St \frac{\partial \mathbf{u}}{\partial t} + \nabla \cdot (\mathbf{u}\mathbf{u}) = -\nabla p + \frac{1}{Re} \nabla^2 \mathbf{u} \quad (2.8)$$

where the Reynolds number, $Re = \rho_l u_r D / \mu_l$, is the ratio of inertial and viscous forces, and the Strouhal number, $St = D / u_r t_r$, is the ratio of the time-dependent inertial force to the convective inertial force. The normal stress boundary condition at the bubble interface becomes

$$p_l - p_v + \frac{1}{We} \kappa_b = \frac{1}{Re} \left(\frac{\partial u_n}{\partial n} \right)_l \quad (2.9)$$

where the Weber number, $We = \rho_l u_r^2 D / \sigma_b$, represents the ratio of the inertial force to the surface tension force. The dimensionless kinematic and tangential stress boundary conditions at the bubble interface and the dimensionless ideal gas law are the same as their dimensional counterparts, Eqs. (2.2), (2.4), and (2.1), with the dimensional variables replaced by their dimensionless forms. The force balance at the flexible tube wall is

$$p_l - \frac{1}{Re} \left(\frac{\partial u_n}{\partial n} \right)_l + \Omega_s \Delta r + \Omega_t \kappa_w = 0 \quad (2.10)$$

where Δr is the dimensionless radial displacement of the wall, dimensionless wall stiffness is

$$\Omega_s = \frac{k_{sp} D}{\rho_l u_r^2} \quad (2.11)$$

and dimensionless wall tension is

$$\Omega_t = \frac{\sigma_w}{\rho_l u_r^2 D} \quad (2.12)$$

In the present study, we consider $D = 36 \mu\text{m}$, a typical value for small arterioles. We compute the velocity scale, u_r , in the system by estimating of the peak velocity of the interface in a manner similar previous bubble expansion models [30,46]. The peak velocity is proportional to the initial bubble pressure and depends on the instantaneous bubble pressure in a nonlinear fashion. One method to estimate the peak velocity is to assume that the initial bubble pressure P_h^* is constant for a short duration Δt ($= 10^{-6}$ s), during which the two liquid columns of length $L_t/2$ are pushed back by the expanding bubble, where L_t denotes the tube length. With this simplification, the approximate peak velocity of the bubble interface is computed as

$$u_r = \frac{P_h^* - P_\infty^*}{L_t \rho_l / 2} \Delta t \quad (2.13)$$

Note that this velocity scale results in a slightly higher Reynolds number than that based on the instantaneous bubble tip velocity during the majority of the bubble lifespan. The corresponding time scale, t_r , is Δt . The velocity scale in Eq. (2.13) is the same scale one would obtain by balancing the time-dependent inertial term with the pressure gradient in the Navier-Stokes equation.

The physics of this bubble-fluid-wall interaction problem are

Table 1 Summary of dimensionless parameters used in the simulations

Case	Re	We	St	Ω_s (stiffness)	Ω_r (wall tension)	Initial pressure P_h	Initial diameter d_i
1	428	6.93	10.5	5×10^{-9}	0.05	176 ($P_h^*=20$ bar)	0.1
2	428	6.93	10.5	5×10^{-9}	0.05	176 ($P_h^*=20$ bar)	0.3
3	428	6.93	10.5	5×10^{-9}	0.05	176 ($P_h^*=20$ bar)	0.5
4	428	6.93	10.5	5×10^{-9}	0.05	176 ($P_h^*=20$ bar)	0.7
5	428	6.93	10.5	5×10^{-9}	0.05	176 ($P_h^*=20$ bar)	0.9

too complex to examine in a single, exhaustive study, and consequently we have focused our attention on the effects of initial bubble diameter, d_i . Each simulation at one set of parameter values required more than 400 CPU hours on an IBM P690 to complete. The relative importance of convective and time-dependent liquid inertia, viscosity, surface tension, initial bubble pressure, initial bubble size, wall stiffness and wall tension is represented by the following dimensionless parameters: Reynolds number, Re, Weber number, We, Strouhal number, St, wall stiffness, Ω_s , wall tension, Ω_r , initial bubble pressure, P_h , and initial bubble size, d_i . This large set of parameters presents a challenge. It is not practical to vary each of the parameters because the exponential increase in the number of simulation cases is prohibitive, given that each individual case is computationally expensive. We have previously investigated the effects of varying Reynolds number, Re, Weber number, We, Strouhal number, St, initial bubble pressure, P_h , and initial bubble size, d_i for a rigid tube wall [30]; we do not examine their effects here.

The principal set of dimensionless parameters used in our rigid wall study [30], supplemented by wall flexibility parameters $\Omega_s = 5 \times 10^{-9}$ and $\Omega_r = 0.05$, is chosen for the simulations herein in order to highlight the impact of the wall flexibility. This parameter set represents typical values in a small arteriole. The only parameter that is varied is the initial bubble diameter, d_i , because our previous study demonstrated that bubble size significantly affects the wall stresses, which is intuitively understandable. The computed cases are summarized in Table 1. Five different bubble diameters are considered, i.e., from 10% to 90% of the tube diameter, in 10% increments. The wall is flexible over its entire length. The physical dimensions and scales underlying the dimensionless parameters are as follows. The tube diameter is $36 \mu\text{m}$, which is the length scale. The tube length is set to be seven times the diameter, i.e., $7 \times 36 \mu\text{m} = 0.252 \text{ mm}$. This value was based on typical lengths of the vessel generations, e.g., the length of the vessel segment between bifurcations [45]. This straight tube model ignores the details of vessel bifurcations and is intended to provide insights into the effects of wall flexibility. The size of the computational domain is 7.0×1.4 , enclosing a tube with diameter of 1.0 and length of 7.0. The present study employed a uniform Cartesian grid of 702×77 that has the same finest resolution as that used in our prior investigation [30] and whose convergence was demonstrated previously.

3 Numerical Method

The model outlined in Sec. 2 constitutes a bubble-fluid-structure interaction problem that includes multiple moving boundaries: a deforming fluid-fluid interface and a flexible fluid-structure boundary. A brief motivation for our numerical method follows. More details of the method and comparison to alternatives are provided elsewhere [30,48]. Accurate prediction of wall and bubble interface positions is essential for the accurate prediction of wall stresses. The boundary element method provides high accuracy for interfacial flows, because the governing equations are transformed to the boundaries, including interfaces [49]. However, applying it to the full Navier-Stokes equations, rather than Stokes flow or potential flow, requires inclusion of approximation terms within the domain [50]. Solution methods for the full

Navier-Stokes equations can be classified as either moving-grid, in which the grid conforms to the physical boundaries and must be regenerated if the boundaries deform, or fixed-grid methods. While moving-grid methods are often effective for steady-state problems, generating new grids at each time step has disadvantages for time-dependent problems and such methods are generally not effective for large boundary deformations in time-dependent problems. For example, steady propagation of an air finger into a liquid-filled flexible channel as a model of airway reopening has been investigated using the finite element method and iterating to determine the steady-state channel shape [41]. Fixed-grid methods include both single domain and multi-domain methods. Single-domain Navier-Stokes solvers smear interfaces and provide a continuous solution across the interfaces [51], both of which may adversely affect the accuracy [48]. Therefore, the computational expense of the highly accurate cut-cell method implemented here is warranted. We have used this method in our previous rigid tube study [30] and briefly describe it here.

We use a fixed-grid, interface-tracking, multi-domain method [52,53], in which interfaces are tracked explicitly by Lagrangian marker particles and cubic B splines that interpolate the marker points are used to calculate the interfacial curvature. Interfaces intersect with the grid and split the computational domain into multiple subdomains. Different governing equations can be specified and solved in separate subdomains to represent fluid or solid conveniently. Using cut cells to conform to the interfaces that are treated sharply to enable a uniform treatment of any moving boundary requires sharp treatment including fluid-fluid interfaces and fluid-solid boundaries. Because subdomains are solved separately, the solutions are discontinuous across the moving boundaries. The method has been validated to assess its accuracy, and is described in detail in previous reports [48,52,53]. A finite-volume, fractional-step method [54–56] is employed to solve the Navier-Stokes equations in the liquid phase. The discretization procedure deals with both Cartesian and trapezoidal cells. The reshaping procedure maintains flux conservation around the interface, so conservation laws are satisfied at all resolvable scales, including the computational cells intersecting with phase boundaries. Consistent interpolation formulas are used to compute the fluxes along the cell surfaces including a linear-quadratic interpolation to handle the non-Cartesian cell faces [48,52,53]. Both inviscid and viscous terms are discretized to create a globally second-order accurate algorithm. For time integration of the Navier-Stokes equations, the convective terms are treated explicitly by a second-order Adams-Bashforth scheme, and the viscous terms are treated semi-implicitly by a Crank-Nicholson scheme. An algebraic multi-grid solver is used to solve the discretized pressure Poisson equation, and avoids the difficulties encountered by the geometric multigrid method in unstructured geometry because the stencil on grid cells cut by the interface is slightly larger than the standard five-point stencil. OpenMP is used to parallelize the computational code.

4 Results and Discussion

The addition of wall flexibility results in a much more complicated flow field than in the rigid wall case. Figure 2 shows the successive snapshots of the streamlines, and bubble and wall

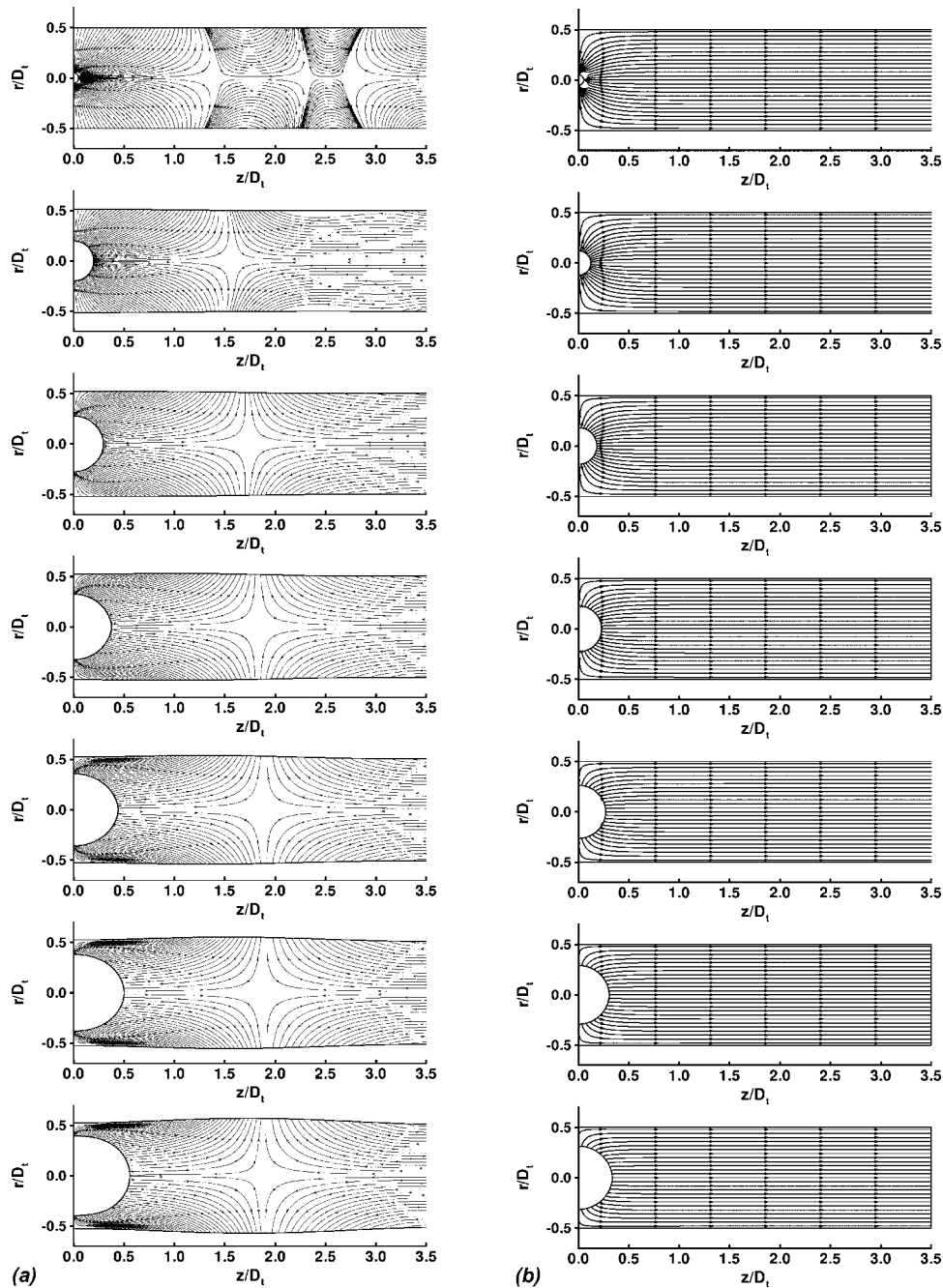


Fig. 2 (a) Bubble and wall shapes, and streamlines at $t=0.004, 0.4, 0.8, 1.2, 1.6, 2.0,$ and 2.4 , for case 1 in Table 1, $Re=427.59, We=6.93, St=10.47, \Omega_s=5 \times 10^{-9}, \Omega_t=0.05, P_h=176.39$ ($P_h^* = 20$ bar), $d_j=0.1$. One dimensionless time unit corresponds to 10.5×10^{-6} s. The bubble is initially spherical with a diameter of 0.1. The bubble shape evolves in time. The horizontal axis is the longitudinal direction, z , of the tube. Only half of the physical domain, $0 \leq z \leq 3.5$, is shown because of symmetry. (b) The same plots for the rigid tube case. The dimensionless parameters are identical to those in (a) except for Ω_s and Ω_t that do not exist in rigid tube case.

shapes for an initial bubble diameter of 0.1. At each time, one or more stagnation fronts separate opposing flows. This is caused by two major driving mechanisms of the flow field. One is the bubble expansion that pushes the fluid away from the bubble and towards the ends of the tube. The other is that the tube wall deformation results in an increase in the tube volume, and, thus “sucks” liquid from the reservoirs into the tube in order to conserve liquid mass. The un-deformed wall position is at $r=0.5$. In the early phases of expansion, the significant deformation of the tube wall occurs near the bubble, and the maximum pressure occurs there. As the bubble

expands further, the bubble pressure decreases due to the increase in bubble volume and the pressure at the stagnation front increases. As a result, the tube bulges outward at the point of the stagnation front. This can be seen in the last two plots in Fig. 2.

The extreme fluid pressure at the tube wall is much smaller when the wall is flexible. This is at the expense of stretching the tube wall, which increases the stresses inside the tube wall compared to the un-stretched configuration. The fluid pressure and shear stress on the tube wall are shown in Fig. 3 for the same times and conditions as the streamlines in Fig. 2. Except at the

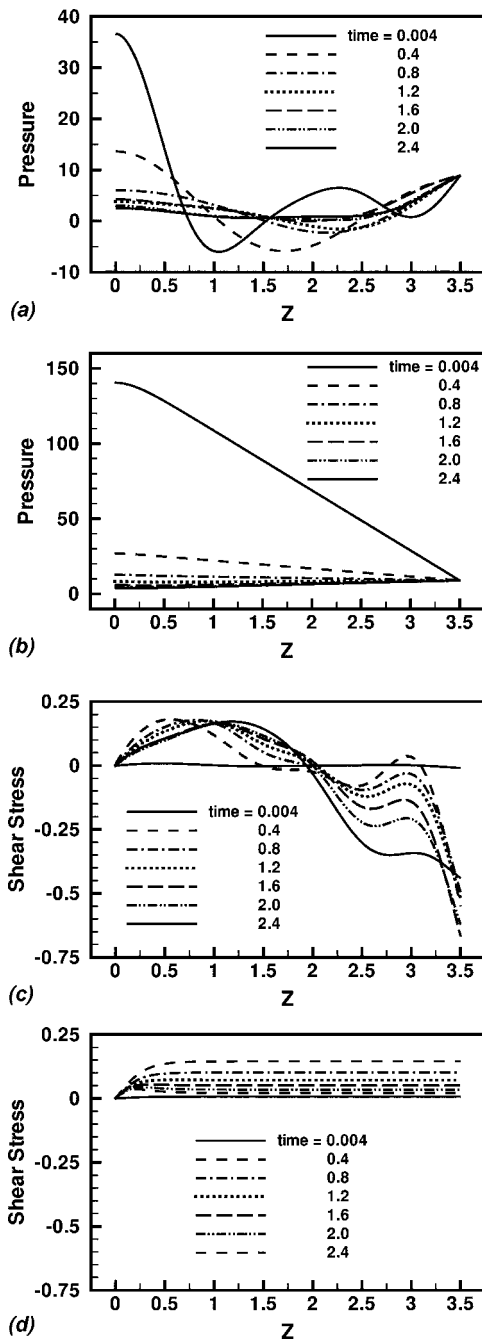


Fig. 3 Comparison of results for pressure (a & b) and shear stress (c & d) on the tube wall between flexible wall (a & c) and rigid wall (b & d) models. The two models share an identical set of parameters: $Re=427.59$, $We=6.93$, $St=10.47$, $P_h=176.39$, and $d_i=0.1$. The flexible wall model has two additional parameters characterizing the wall flexibility. The horizontal axis is the longitudinal direction, z , of the tube. Only half of the physical domain, $0 \leq z \leq 3.5$, is shown because of symmetry. The dimensional stress is 11338.8 N/m^2 per dimensionless unit.

beginning of the expansion, the fluid pressure inside the tube is always smaller than the fixed ambient pressure at the tube entrances owing to the expanding tube volume. The pressure near the stagnation point at $z \sim 2.0$ increases over time and contributes to the deformation of the tube at that location. The shear stress exhibits a sign reversal because of complicated velocity field, which includes stagnation points, non-zero wall velocities, and flow reversal. Additional insights can be obtained by comparing

the current flexible wall results with those for the rigid wall. The expansion of the bubble in a flexible tube does not result in the “saddle” shape of the bubble at its center, $z=0$ that was observed in rigid tube cases [30]. In Fig. 3, the pressure and shear stress results are shown side by side. Although the distribution of shear stress is different in the rigid and flexible tube models, the overall magnitude of the shear stress is similar for both, suggesting that the computationally less expensive rigid wall model might be useful in predicting the shear stress magnitude in vessels that are not truly rigid. The time of transient evolution from the initial high pressure to ambient level is an order of magnitude smaller in the flexible wall case. This indicates the flexible wall not only reduces the extreme pressure but also shortens the impact time. The reason for this reduction in time is that the flexible tube wall expands quickly, reducing the pressure within the bubble that is driving the bubble expansion. One can interpret the dimensionless wall stiffness and tension, Ω_s and Ω_r , as ratios of stiffness or tension force to inertial force. Both of these are small, indicating that less force is needed to overcome either wall stiffness or tension than is needed to overcome fluid inertia, and consequently the wall deforms relatively easily. In the rigid wall can be thought of as the limit of infinite wall stiffness, $\Omega_s \rightarrow \infty$, and in that case the bubble expansion only moves the fluid.

To assess the importance of wave propagation along the flexible tube wall to the resulting fluid-wall dynamics, we estimated the wave speed based on classical one-dimensional analysis [36,45,47,57] that ignores wall tension, which is relatively weak here. Although this wave speed calculation relies on a number of idealized assumptions, it provided a coarse estimate of wave speed, $c = \sqrt{A^* / \rho dP^* / dA^*}$, where A^* is the cross-sectional area of the tube and, as previously, P^* is pressure. $A^* dA^* / dP^*$ indicates the distensibility of the elastic tube [45]. Rewriting dP^* / dA^* in terms of the tube wall spring constant, k_{sp} , and combining this expression with Eq. (2.11), we obtain a ratio of the wave speed to the velocity scale of the flow, $c / u_r = \sqrt{\Omega_s} / 2$. For the arteriole parameter values considered here, $c / u_r \ll 1$ indicating that the bubble expansion occurs more rapidly than wave propagation along the vessel wall. In classical examinations of steady flow in collapsible tubes [36,37], fluid velocities that exceed the wave speed led to flow limitation and tube collapse. Here, the flow is extremely unsteady, and the expansion of the bubble induces high fluid pressures that oppose tube collapse. Additionally, the expansion of the bubble is driving the flow and it induces local expansion of the tube. However, there does appear to be a limitation on pushing the liquid out through the ends of the tube. In fact, the bubble expansion induces tube wall expansion that is so fast as to induce in flow at the tube ends. Less distensible tube walls have higher wave speeds, and presumably would allow out flow at the tube ends if the tube is sufficiently stiff because it would be easier for the expanding bubble to push the liquid out of the tube than to expand the tube wall. The limit of zero distensibility is the rigid tube wall of our previous investigation [30], in which out flow always occurred during bubble expansion. The subsequent diffusion of gas into the bubble, which is not considered here, occurs over a sufficiently long time that the bubble growth due to uptake of gas from the surrounding blood may interact with wave propagation/reflection in actual vessels. However, it appears that for the rapid expansion considered here that the neglect of wave reflection at vessel bifurcations does not have a significant impact on the resulting behavior. The small value of c / u_r can also be thought of as an indication of the long time (compared to the time scale of the bubble expansion) required for the tube wall to overcome fluid inertia and return to its original shape at a particular location once it is deformed. As noted in the previous paragraph, the small value of Ω_s here indicates that the tube walls are relatively easy to distend. This is consistent with the wave speed analysis, and the observation that the expansion of the walls reduces the driving pressure and expansion time of the bubble.

For larger values of d_i , the computations were stopped when the

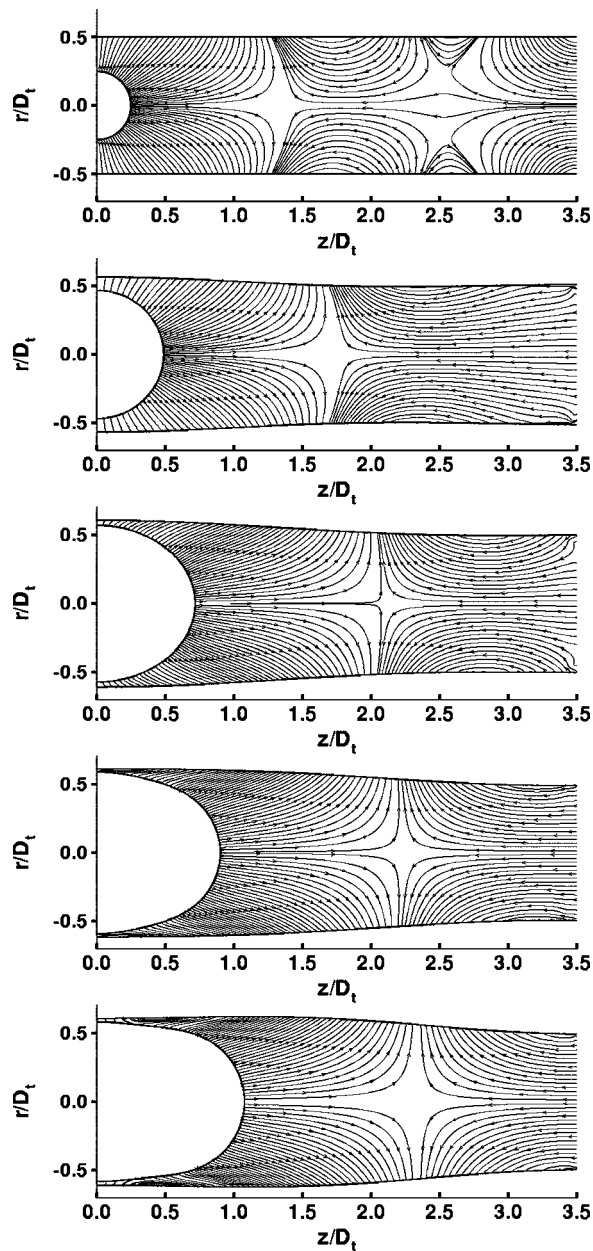


Fig. 4 Bubble and wall shapes, and streamlines at $t=0.004, 0.4, 0.8, 1.2,$ and 1.6 for case 3 in Table 1, $Re=427.59, We=6.93, St=10.47, \Omega_s=5 \times 10^{-9}, \Omega_t=0.05, P_h=176.39,$ and $d_i=0.5$. Only half of the physical domain, $0 \leq z \leq 3.5$, is shown because of symmetry.

bubble interface moved within five computational grid cells of the vessel wall, as further computations became time consuming and it was assumed that the bubble would contact the wall soon after this time. This criterion is based on our previous resolution study [30]. The maximum fluid stresses occur at early times during the bubble expansion before the bubble approaches the wall, and further computations do not provide additional information regarding the maximum fluid pressure at the wall. This criterion does not allow time to advance far enough for the maximum wall shear stress to be obtained for $d_i=0.7$ and 0.9 , but allows investigation of the maximum wall pressure and behavior of the flow and wall stress. Additionally, this resulted in the halting of the computations before the bubble reached its maximum volume and before oscillations of the bubble could occur. In the rigid tube wall case, the bubble expanded past its equilibrium size due to inertia of the

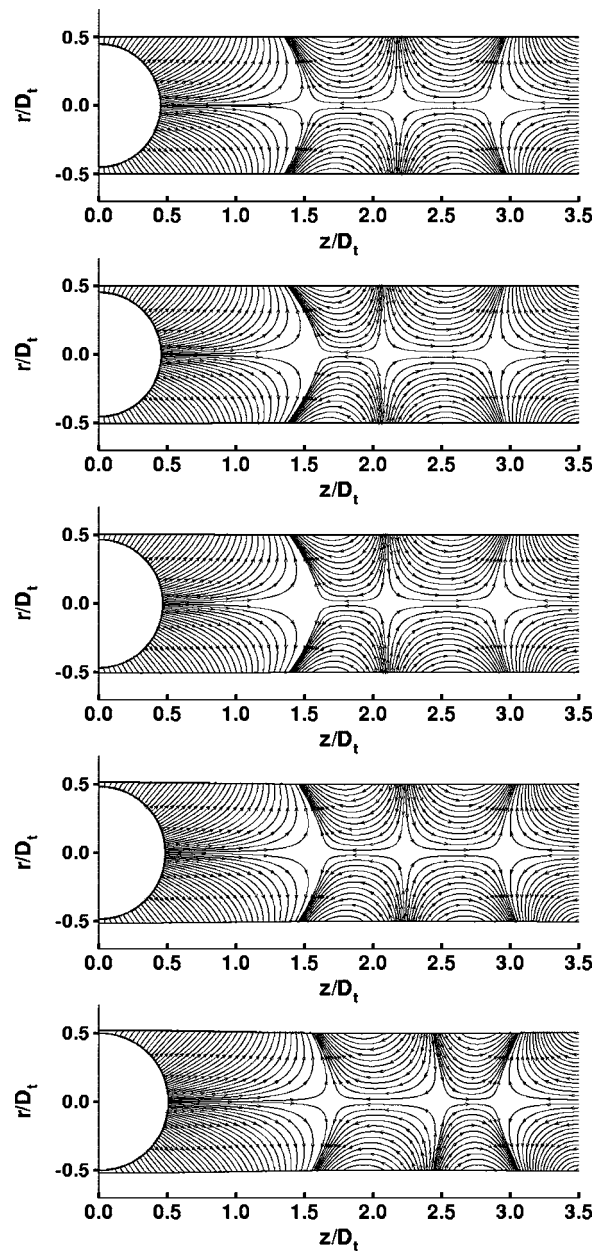


Fig. 5 Bubble and wall shapes, and streamlines at $t=0.004, 0.04, 0.08, 0.12,$ and 0.16 for case 5 in Table 1, $Re=427.59, We=6.93, St=10.47, \Omega_s=5 \times 10^{-9}, \Omega_t=0.05, P_h=176.39,$ and $d_i=0.9$. Only half of the physical domain, $0 \leq z \leq 3.5$, is shown because of symmetry.

surrounding liquid and then oscillated with decaying amplitude until reaching equilibrium. The liquid viscosity damped the oscillations. Because our interest was investigating the potential of vessel damage, we did not investigate the oscillations, which resulted in lower stresses.

Larger initial bubbles result in larger deformation of the vessel wall near the bubble, and produce complicated flow patterns that include stagnation points. Streamlines for $d_i=0.5$, and 0.9 are shown in Figs. 4 and 5, respectively. The corresponding wall pressures and shear stresses are shown in Figs. 6 and 7. Note that for the larger initial bubble diameter, $d_i=0.9$, the time between streamline plots is smaller (Fig. 5) than in the streamline plots for the other initial bubble diameters (Figs. 2 and 4), $d_i=0.1$ and 0.5 , because the computations were stopped at earlier times. However, the magnitude of the shear stress is larger than that for an initial

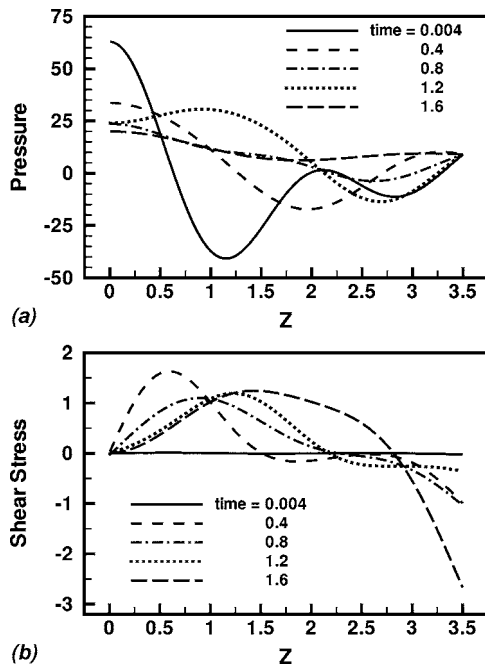


Fig. 6 (a) Pressure and (b) shear stress on the tube wall at various times for case 3 in Table 1, $Re=427.59$, $We=6.93$, $St=10.47$, $\Omega_s=5 \times 10^{-9}$, $\Omega_t=0.05$, $P_h=176.39$, and $d_i=0.5$. Only half of the physical domain, $0 \leq z \leq 3.5$, is shown because of symmetry. The dimensional stress is 11338.8 N/m^2 per dimensionless unit.

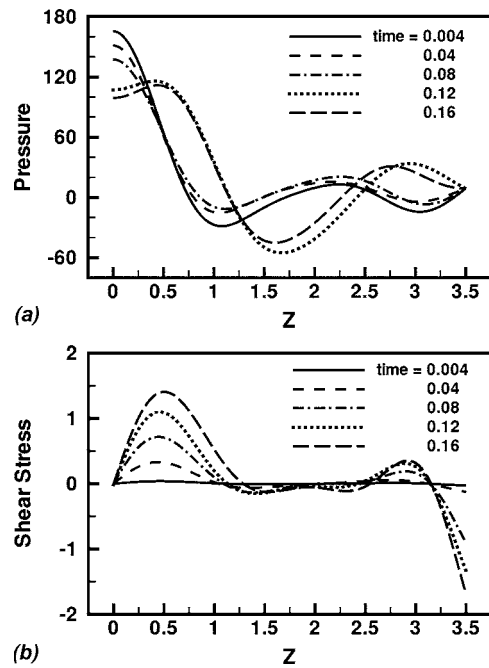


Fig. 7 (a) Pressure and (b) shear stress on the tube wall at various times for case 5 in Table 1, $Re=427.59$, $We=6.93$, $St=10.47$, $\Omega_s=5 \times 10^{-9}$, $\Omega_t=0.05$, $P_h=176.39$, and $d_i=0.9$. Only half of the physical domain, $0 \leq z \leq 3.5$, is shown because of symmetry. The dimensional stress is 11338.8 N/m^2 per dimensionless unit.

bubble diameter of 0.1. The reversal in direction of liquid flow along the tube results in both positive and negative values of the wall shear stress.

The peak pressure and peak shear stress are both higher for larger initial bubble diameters, d_i . For brevity, streamlines, pressures, and shear stresses are not shown for $d_i=0.3$ and 0.7 . These were computed and the peak fluid pressure at the wall for each is compared to those of the other d_i values in Fig. 8. The elevated wall pressures are significant, but are short in duration, $t < 0.4$ (Figs. 3, 6, and 7). For all d_i , multiple stagnation fronts occur at early times. As time progresses, only a single stagnation point remains on each side of the bubble, for $d_i=0.1$ and 0.5 . Similar behavior would be expected at later times for $d_i=0.9$. As for $d_i=0.1$ and 0.3 , the pressure ahead of the expanding bubble increases in time near the stagnation point and eventually leads to expansion of the tube wall there. As the bubble expands, mass conservation requires that the tube walls expand and/or liquid exit the tube ends in order to accommodate the increased bubble volume. Tube walls with relatively low spring constants and negligible mass are easy to expand compared to overcoming the liquid inertia and viscous resistance needed to expel liquid from the ends of the tube. The bubble expansion expands the tube wall relatively quickly near the bubble, leading to in flow at the ends of the tube.

For all d_i considered in this study, the wall shear stress is initially zero for all z because the liquid is initially at rest. As time increases and the bubble interface moves closer to the wall, the peak shear stress increases. As time progresses further, the bubble volume increases resulting in a decreased bubble pressure. This in turn results in a decreased interfacial velocity, which results in lower peak shear stresses (reduced by approximately half) at later times. This is evident for $0.1 \leq d_i \leq 0.5$, when $t > 1.0$. At very long times (not shown), the bubble reaches its equilibrium configuration and does not induce flow or shear stress.

4.1 Implications for Gas Embolotherapy. The results demonstrate that tube wall flexibility can significantly modify the wall

stresses that result from acoustic vaporization of intravascular perfluorocarbon droplets compared to the rigid tube wall. This finding suggests activation of droplets in larger, more flexible vessels will likely reduce the risk of vessel rupture or damage to the endothelium compared to activation in smaller and stiffer vessels. However, this reduced risk of vessel injury during droplet vaporization comes at the expense of forming bubbles further away from the desired location of bubble sticking, i.e., the tumor microvessels, and, therefore, increases the risk of collateral tissue infarction, an unwanted result. Selection of vessels for the vaporization of droplets will require careful consideration of both risks in order to optimize efficacy.

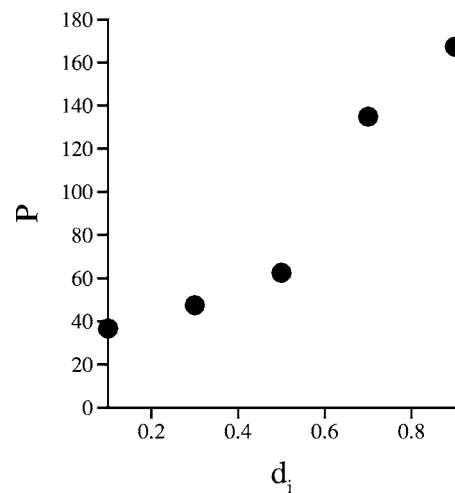


Fig. 8 The maximum pressure on the tube wall versus d_i at $t=0.004$. $Re=427.59$, $We=6.93$, $St=10.47$, $\Omega_s=5 \times 10^{-9}$, $\Omega_t=0.05$, $P_h=176.39$.

4.2 Model Limitations. As with the rigid tube cases, quantitative relevance of the simulation results is dictated by the specified initial bubble pressure which is a collective modeling parameter of the phase change. This initial pressure is an approximation of several concurrent dynamic and thermal physical mechanisms in the droplet vaporization process. There is no direct correspondence between this initial bubble pressure and a readily measured physical quantity. Experimental studies are being conducted in our group in order to provide appropriate initial pressure values to calibrate the modeling parameter. The calibration procedure is described in Ye and Bull [30]. As noted in Sec. 1 and 2, ADV appears to occur due to disruption of the albumin shell encapsulating the droplet, and consequently we have assumed that the gas phase can be represented by the isothermal ideal gas law. There may potentially be other modes of vaporization, such as cavitation within the liquid droplet or in the blood surrounding the droplet. Future experiments will provide important information on the process and will facilitate incorporation of these details into future computational models.

The present model for a flexible wall is rather simplified in order to be able to investigate the effect of adding fluid-structure dynamics to a system that is dominated by fluid-fluid interface dynamics. The current investigation has neglected wall mass and dampening, and vessel asymmetries and bifurcations. Tube models that more closely resemble blood vessel properties may be needed to account for the inertia effects associated with vessel mass and viscoelastic properties of blood vessels. Our estimate of k_{sp} was chosen to match arteriole values, but future work could investigate the flows that result from considering a wider range of vessel sizes and locations for droplet vaporization. The resulting flow and stresses could be quite different in other vessels. For example, values of the dimensionless parameters (based on bubble expansion and typical vessel parameters [45]) in arteries can reach values as high as $Re=O(10,000)$, $We=O(10,000)$, $St=O(10,000)$, $\Omega_s=O(10)$, and $\Omega_t=O(10)$. In capillaries, we might expect $Re=O(10)$, $We=O(1)$, and $St=O(1)$. Surrounding tissue can result in a wide range of wall stiffness and tension parameters, as well as contribute to wall mass and dampening. Likewise, 6–32 μm droplets will result in d_i values that range from $O(10^{-4})$ to $O(1)$. The bioeffects resulting from vaporization of small droplets in large vessels will depend on the proximity of the droplet to the vessel wall. Vessel bifurcations and junctions can lead to reflection of pressure waves propagating along the vessel walls due to the pulsatility of blood flow, an effect we have neglected by considering idealized boundary conditions at the ends of the model vessel. The geometry of junctions and length of the vessel segment between junctions are expected to affect the resulting wall stresses. The length of vessel segments between bifurcations in the microcirculation is typically the same order that we have considered here, e.g., $L_i/D=7.0$ [45,58], and, therefore, we did not investigate the effects of small length differences on the results in this work. The initial location of the droplet at the center of the tube is also an idealization compared to the physiologic situation. Vaporization of the droplet at other locations, as well as the heterogeneity of real vessel walls, is expected to result in asymmetric flow and deformation patterns in the actual situation.

Although we neglect background flow in our analysis because typical arteriole blood velocities are much smaller than the velocity associated with the rapidly expanding bubble, background blood flow and vessel wall oscillations due to flow pulsatility could be significant in larger vessels. Sufficiently strong flow could modify the behavior of the expanding bubble by deforming the albumin-encapsulated droplet such that the initial bubble shape is not actually spherical. We have modeled blood as a Newtonian fluid, and neglected the presence of its cellular components. For vaporization of droplets in capillaries, bubble interaction with individual blood cells may affect the resulting flow and stress fields. For droplet vaporization in large vessels, non-Newtonian constitutive equations may provide useful information

in future investigations. Nevertheless, the present study provides a first step in understanding the effects of wall flexibility on bubble expansion in a liquid-filled tube and serves to guide our developing gas embolotherapy work.

5 Conclusions

A fluid-structure interaction model is presented to study unsteady, microbubble expansion in a flexible tube in order to assess the risk of vessel damage from acoustic droplet vaporization in a potential gas embolotherapy technique. The model consists of a bubble inside a flexible tube open to liquid reservoirs. An evolving fluid-fluid interface and a fluid-structure boundary are solved as part of the solution in the system. The liquid is governed by viscous, incompressible Navier-Stokes equations while the bubble is modeled as ideal gas. The flexibility of the tube wall is modeled by stiffness and tension components. The numerical method is a fixed-grid, interface-tracking, multi-domain method that treats both fluid-fluid and fluid-solid boundaries sharply to accurately resolve the interface evolution.

This report is the first to present results of the stresses on a flexible tube wall induced by a bubble expanding inside the tube, and demonstrates that the flow physics are very complex and highly transient. A stagnation front of flows, a wave behavior of the tube structure, and bubble interface evolution are key features characterizing the process. Significant differences in stress and flow are observed when the tube wall is flexible. The extreme stress and the initial time period in which the pressure reduces from its peak to ambient level in a flexible tube are much smaller than those in a rigid tube. In our developmental gas embolotherapy, acoustic activation of droplets in larger, more flexible vessels may be less likely to damage or rupture vessels than activation in smaller and stiffer vessels.

Acknowledgment

This work was supported by NIH Grant No. EB003541 and NSF Grant No. BES-0301278. Computational resources were provided by the National Computational Science Alliance under BIO030007N utilizing an IBM P690 parallel computer. The authors thank Dr. J. Brian Fowlkes and Dr. Oliver D. Kripfgans for valuable discussions.

References

- [1] Bull, J. L., 2005, "Cardiovascular Bubble Dynamics," *Crit. Rev. Biomed. Eng.*, **33**(4), pp. 299–346.
- [2] Halpern, D., Jiang, Y., and Himm, J. F., 1999, "Mathematical Model of Gas Bubble Evolution in a Straight Tube," *ASME J. Biomech. Eng.*, **121**(5), pp. 505–513.
- [3] Cavanagh, D. P., and Eckmann, D. M., 1999, "Interfacial Dynamics of Stationary Gas Bubbles in Flows in Inclined Tubes," *J. Fluid Mech.*, **398**, pp. 225–244.
- [4] Eckmann, D. M., and Cavanagh, D. P., 2003, "Bubble Detachment by Diffusion-Controlled Surfactant Adsorption," *Colloids Surf., A*, **227**(1–3), pp. 21–33.
- [5] Eckmann, D. M., Cavanagh, D. P., and Branger, A. B., 2001, "Wetting Characteristics of Aqueous Surfactant-Laden Drops," *J. Colloid Interface Sci.*, **242**(2), pp. 386–394.
- [6] Eckmann, D. M., and Diamond, S. L., 2004, "Surfactants Attenuate Gas Embolism-Induced Thrombin Production," *Anesthesiology*, **100**(1), pp. 77–84.
- [7] Branger, A. B., and Eckmann, D. M., 1999, "Theoretical and Experimental Intravascular Gas Embolism Absorption Dynamics," *J. Appl. Physiol.*, **87**(4), pp. 1287–1295.
- [8] Branger, A. B., and Eckmann, D. M., 2002, "Accelerated Arteriolar Gas Embolism Reabsorption by an Exogenous Surfactant," *Anesthesiology*, **96**(4), pp. 971–979.
- [9] Branger, A. B., Lambertsen, C. J., and Eckmann, D. M., 2001, "Cerebral Gas Embolism Absorption During Hyperbaric Therapy: Theory," *J. Appl. Physiol.*, **90**(2), pp. 593–600.
- [10] Muth, C. M., and Shank, E. S., 2000, "Primary Care: Gas Embolism," *N. Engl. J. Med.*, **342**(7), pp. 476–482.
- [11] Boehm, T., Folkman, J., Browder, T., and O'Reilly, M. S., 1997, "Antiangiogenic Therapy of Experimental Cancer Does not Induce Acquired Drug Resistance," *Nature (London)*, **390**, pp. 404–407.
- [12] Di Segni, R., Young, A. T., Zhong, Q., and Castaneda-Zuniga, W. R., 1997, "Embolotherapy: Agents, Equipment, and Techniques," *Interventional Radi-*

- ology, W. R. Castaneda-Zuniga, Williams and Wilkins, Baltimore, pp. 81–84.
- [13] Nakagawa, N., and Castaneda-Zuniga, W. R., 1997, “Transcatheter Chemoembolization for Hepatocellular Carcinoma and Other Promising Transarterial Therapies,” *Interventional Radiology*, W. R. Castaneda-Zuniga, Williams and Wilkins, Baltimore.
- [14] Nakamura, H., Hashimoto, T., Oi, H., and Sawada, S., 1989, “Transcatheter Oily Chemoembolization of Hepatocellular-Carcinoma,” *Radiology*, **170**(3), pp. 783–786.
- [15] Kripfgans, O. D., Fabiilli, M. L., Carson, P. L., and Fowlkes, J. B., 2004, “On the Acoustic Vaporization of Micrometer-Sized Droplets,” *J. Acoust. Soc. Am.*, **116**(1), pp. 272–281.
- [16] Kripfgans, O. D., Fowlkes, J. B., Miller, D. L., Eldevik, O. P., and Carson, P. L., 2000, “Acoustic Droplet Vaporization for Therapeutic and Diagnostic Applications,” *Ultrasound Med. Biol.*, **26**(7), pp. 1177–1189.
- [17] Kripfgans, O. D., Fowlkes, J. B., Woydt, M., Eldevik, O. P., and Carson, P. L., 2002, “In Vivo Droplet Vaporization for Occlusion Therapy and Phase Aberration Correction,” *IEEE Trans. Ultrason. Ferroelectr. Freq. Control*, **49**(6), pp. 726–738.
- [18] Calderon, A. J., and Bull, J. L., 2004, “Homogeneity of Bubble Transport Through a Bifurcation for Gas Embolotherapy,” *FASEB J.*, **18**(4), p. A373.
- [19] Calderon, A. J., Fowlkes, J. B., and Bull, J. L., 2005, “Bubble Splitting in Bifurcating Tubes: A Model Study of Cardiovascular Gas Emboli Transport,” *J. Appl. Physiol.*, **99**, pp. 479–487.
- [20] Eshpuniyani, B., Fowlkes, J. B., and Bull, J. L., 2005, “A Bench Top Experimental Model of Bubble Transport in Multiple Arteriole Bifurcations,” *Int. J. Heat Fluid Flow*, **26**(6), pp. 865–872.
- [21] Skyba, D. M., Price, R. J., Linka, A. Z., Skalak, T. C., and Kaul, S., 1998, “Direct in Vivo Visualization of Intravascular Destruction of Microbubbles by Ultrasound and its Local Effects on Tissue,” *Circulation*, **98**(4), pp. 290–293.
- [22] Song, J., Cotler, P. S., Klibanov, A. L., Kaul, S., and Price, R. J., 2004, “Microvascular Remodeling and Accelerated Hyperemia Blood Flow Restoration in Arterially Occluded Skeletal Muscle Exposed to Ultrasonic Microbubble Destruction,” *Am. J. Physiol. Heart Circ. Physiol.*, **287**, pp. H2754–H2761.
- [23] Song, J., Qi, M., Kaul, S., and Price, R. J., 2002, “Stimulation of Arteriogenesis in Skeletal Muscle by Microbubble Destruction With Ultrasound,” *Circulation*, **106**(12), pp. 1550–1555.
- [24] Nerem, R. M., 1993, “Hemodynamics and the Vascular Endothelium,” *ASME J. Biomech. Eng.*, **115**(4), pp. 510–514.
- [25] Chiu, J. J., Wang, D. L., Chien, S., Skalak, R., and Usami, S., 1998, “Effects of disturbed flow on endothelial cells,” *ASME J. Biomech. Eng.*, **120**(1), pp. 2–8.
- [26] Helmlinger, G., Berk, B. C., and Nerem, R. M., 1995, “Calcium Responses Of Endothelial-Cell Monolayers Subjected to Pulsatile and Steady Laminar-Flow Differ,” *Am. J. Physiol.: Cell Physiol.*, **38**(2), pp. C367–C375.
- [27] Davies, P. F., Barbee, K. A., Volin, M. V., Robotewskyj, A., Chen, J., Joseph, L., Griem, M. L., Wernick, M. N., Jacobs, E., Polacek, D. C., DePaola, N., and Barakat, A. I., 1997, “Spatial Relationships in Early Signaling Events of Flow-Mediated Endothelial Mechanotransduction,” *Annu. Rev. Physiol.*, **59**, pp. 527–549.
- [28] Nerem, R. M., Harrison, D. G., Taylor, W. R., and Alexander, R. W., 1993, “Hemodynamics and Vascular Endothelial Biology,” *J. Cardiovasc. Pharmacol.*, **21**, pp. S6–S10.
- [29] Badimon, L., Badimon, J. J., Penny, W., Webster, M. W., Chesebro, J. H., and Fuster, V., 1992, “Endothelium and Atherosclerosis,” *J. Hypertens.*, **10**, pp. S43–S50.
- [30] Ye, T., and Bull, J. L., 2004, “Direct Numerical Simulations of Micro-Bubble Expansion in Gas Embolotherapy,” *ASME J. Biomech. Eng.*, **126**(6), pp. 745–759.
- [31] Grotberg, J. B., 1994, “Pulmonary Flow and Transport Phenomena,” *Annu. Rev. Fluid Mech.*, **26**, pp. 529–571.
- [32] Grotberg, J. B., 2001, “Respiratory Fluid Mechanics and Transport Processes,” *Annu. Rev. Biomed. Eng.*, **3**, pp. 421–457.
- [33] Grotberg, J. B., and Jensen, O. E., 2004, “Biofluid Mechanics in Flexible Tubes,” *Annu. Rev. Fluid Mech.*, **36**, pp. 121–147.
- [34] Ku, D. N., 1997, “Blood Flow in Arteries,” *Annu. Rev. Fluid Mech.*, **29**, pp. 399–434.
- [35] Kamm, R. D., and Pedley, T. J., 1989, “Flow in Collapsible Tubes: A Brief Review,” *ASME J. Biomech. Eng.*, **111**, pp. 177–179.
- [36] Shapiro, A. H., 1977, “Steady Flow in Collapsible Tubes,” *ASME J. Biomech. Eng.*, **99**, pp. 126–147.
- [37] Dawson, S. V., and Elliott, E. A., 1977, “Wave-Speed Limitation on Expiratory Flow—A Unifying Concept,” *J. Appl. Physiol.: Respir., Environ. Exercise Physiol.*, **43**(3), pp. 498–515.
- [38] Bull, J. L., Reikert, C. A., Tredici, S., Komori, E., Frank, E. L., Brant, D. O., Grotberg, J. B., and Hirschl, R. B., 2005, “Flow Limitation in Liquid-Filled Lungs: Effects of Liquid Properties and Lung Compliance,” *ASME J. Biomech. Eng.*, **127**(4), pp. 630–636.
- [39] Gaver, D. P., Halpern, D., Jensen, O. E., and Grotberg, J. B., 1996, “The Steady Motion of a Semi-Infinite Bubble Through a Flexible-Walled Channel,” *J. Fluid Mech.*, **319**, pp. 25–65.
- [40] Howell, P. D., Waters, S. L., and Grotberg, J. B., 2000, “The Propagation of a Liquid Bolus Along a Liquid-Lined Flexible Tube,” *J. Fluid Mech.*, **406**, pp. 309–335.
- [41] Heil, M., 2000, “Finite Reynolds Number Effects in the Propagation of an Air Finger Into a Liquid-Filled Flexible-Walled Channel,” *J. Fluid Mech.*, **424**, pp. 21–44.
- [42] Jensen, O. E., Horsburgh, M. K., Halpern, D., and Gaver, D. P., 2002, “The Steady Propagation of a Bubble in a Flexible-walled Channel: Asymptotic and Computational Models,” *Phys. Fluids*, **14**(2), pp. 443–457.
- [43] Hazel, A. L., and Heil, M., 2003, “Three-Dimensional Airway Reopening: The Steady Propagation of a Semi-Infinite Bubble Into a Buckled Elastic Tube,” *J. Fluid Mech.*, **478**, pp. 47–70.
- [44] Naire, S., and Jensen, O. E., 2003, “An Asymptotic Model of Unsteady Airway Reopening,” *ASME J. Biomech. Eng.*, **125**(6), pp. 823–831.
- [45] Fung, Y. C., 1997, *Biomechanics: Circulation*, Springer, New York.
- [46] Ory, E., Yuan, H., Prosperetti, A., Popinet, S., and Zaleski, S., 2000, “Growth and Collapse of a Vapor Bubble in a Narrow Tube,” *Phys. Fluids*, **12**(6), pp. 1268–1277.
- [47] Atabek, H. B., and Lew, H. S., 1966, “Wave Propagation Through a Viscous Incompressible Fluid Contained in an Initially Stressed Elastic Tube,” *Biophys. J.*, **6**(4), pp. 481–503.
- [48] Ye, T., Shyy, W., Tai, C. F., and Chung, J. N., 2004, “Assessment of Sharp- and Continuous-Interface Methods for Drop in Static Equilibrium,” *Comput. Fluids*, **33**(7), pp. 917–926.
- [49] Pozrikidis, C., 2001, “Interfacial Dynamics for Stokes Flow,” *J. Comput. Phys.*, **169**, pp. 250–301.
- [50] Power, H., and Wrobel, L. C., 1995, *Boundary Integral Methods in Fluid Mechanics*, Computational Mechanics, Southampton.
- [51] Brackbill, J. U., Kothe, D. B., and Zemach, C., 1992, “A Continuum Method for Modeling Surface-Tension,” *J. Comput. Phys.*, **100**(2), pp. 335–354.
- [52] Ye, T., Mittal, R., Udaykumar, H. S., and Shyy, W., 1999, “An Accurate Cartesian Grid Method for Viscous Incompressible Flows With Complex Immersed Boundaries,” *J. Comput. Phys.*, **156**(2), pp. 209–240.
- [53] Ye, T., Shyy, W., and Chung, J. N., 2001, “A Fixed-Grid, Sharp-Interface Method for Bubble Dynamics and Phase Change,” *J. Comput. Phys.*, **174**(2), pp. 781–815.
- [54] Chorin, A. J., 1968, “Numerical Solution of Navier-Stokes Equations,” *Math. Comput.*, **22**(104), pp. 745–762.
- [55] Kim, J., and Moin, P., 1985, “Application of a Fractional-Step Method to Incompressible Navier-Stokes Equations,” *J. Comput. Phys.*, **59**(2), pp. 308–323.
- [56] Zang, Y., Street, R. L., and Koseff, J. R., 1994, “A Non-Staggered Grid, Fractional Step Method for Time-Dependent Incompressible Navier-Stokes Equations in Curvilinear Coordinates,” *J. Comput. Phys.*, **114**(1), pp. 18–33.
- [57] Pedley, T. J., 1980, *The Fluid Mechanics of Large Blood Vessels*, Cambridge University Press, Cambridge.
- [58] Fung, Y. C., and Zweifach, B. W., 1971, “Microcirculation—Mechanics of Blood Flow in Capillaries,” *Annu. Rev. Fluid Mech.*, **3**, pp. 189–210.